Supplementary Information (SI) for Journal of Materials Chemistry A.

Supporting Information

Structural Incommensurability Drives Ultralow Lattice Thermal Conductivity in Misfit Layered $(BiSe)_{1.23}CrSe_2$

Anil Kumar B. M.,[a] Shuva Biswas,[b] Sambit Jena,[c] Pranav Negi,[d] Dirtha Sanyal,[e,f]
Banasree Sadhukhan[c] and Satya N. Guin*[a]

[a] *Department of Chemistry, Birla Institute of Technology and Science Pilani, Hyderabad Campus, Jawahar Nagar, Hyderabad 500078, India*

[b] *New Chemistry Unit, Jawaharlal Nehru Centre for Advanced Scientific Research (JNCASR), Jakkur P.O., Bengaluru 560064, India*

[c] *Department of Physics, Ecole Centrale School of Engineering, Mahindra University, Hyderabad 500043, India*

[d] *Department of Chemistry, Indian Institute of Science Education and Research Bhopal, Bhopal 462066, India*

[e] *Variable Energy Cyclotron Centre, 1/AF Bidhannagar, Kolkata 700064, India*

[f] *Homi Bhabha National Institute, Training School Complex, Anushakti Nagar,*

Mumbai 400094, India

*Email: *satyanarayan.g@hyderabad.bits-pilani.ac.in*

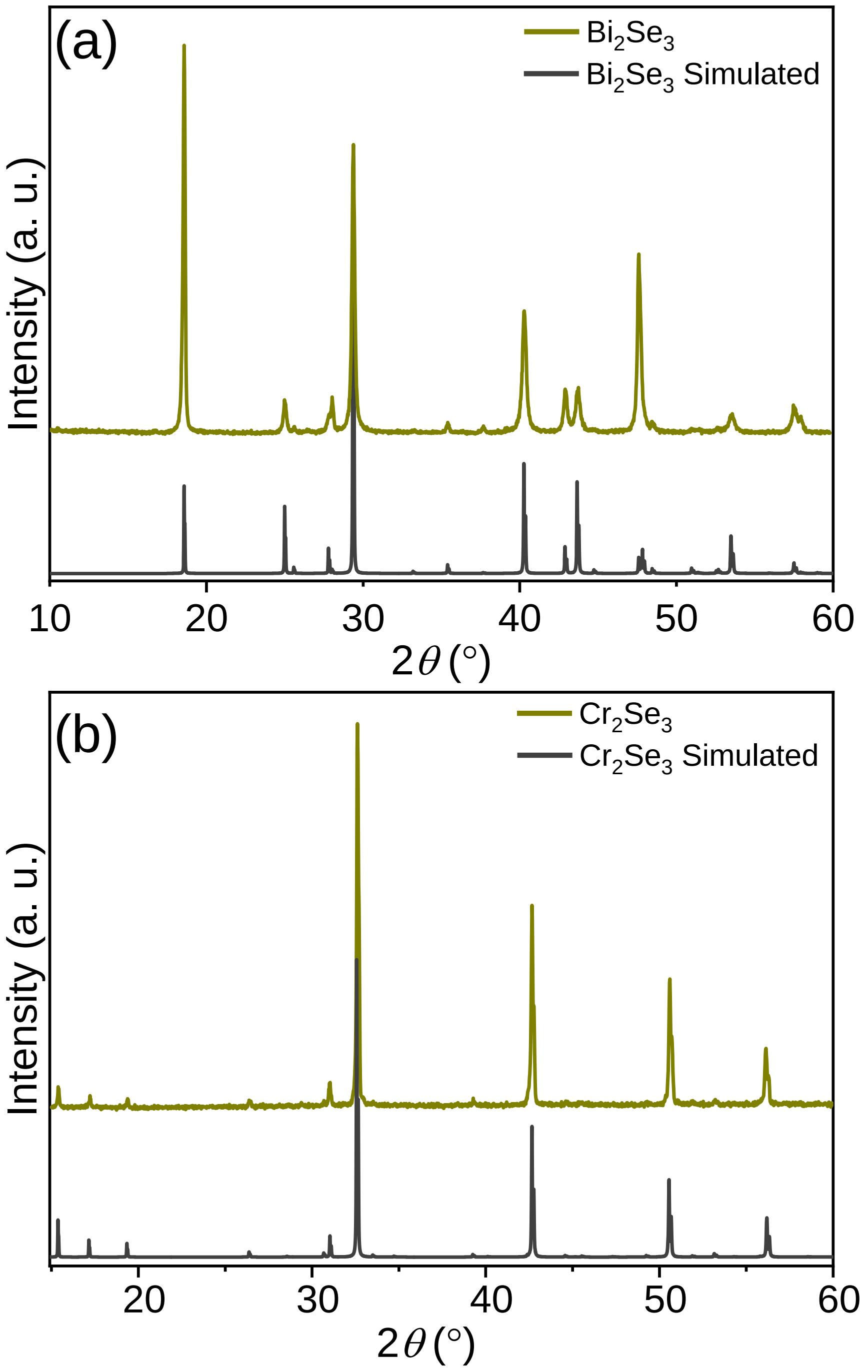

Fig. S1 Room temperature PXRD pattern of (a) Bi_2Se_3 and (b) Cr_2Se_3 plotted with the simulated patterns (COD: 00-901-1965 and COD: 00-152-7062), respectively, showing the phase purity binary mixtures used to synthesise $(BiSe)_{1.23}CrSe_2$ as described by Clarke et.al.[1]

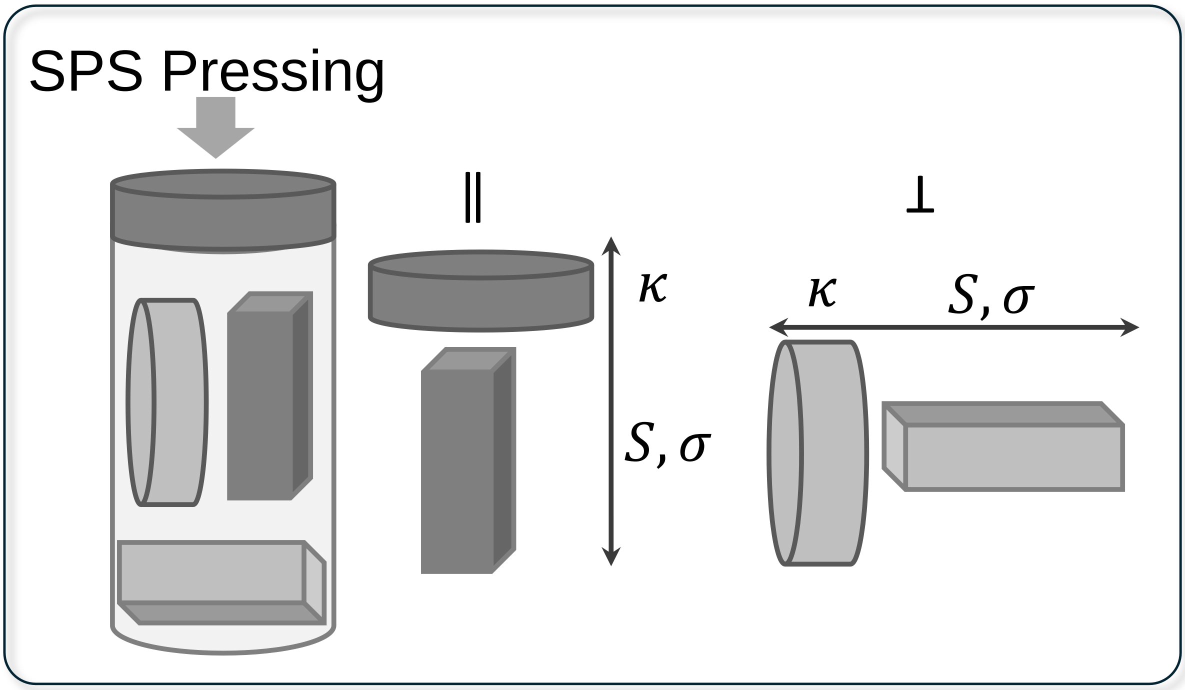

Fig. S2 A schematic illustrating the preparation of standard bars and coins from the SPS'ed sample for measuring thermal and electrical transport properties, both parallel and perpendicular to the SPS pressing direction.

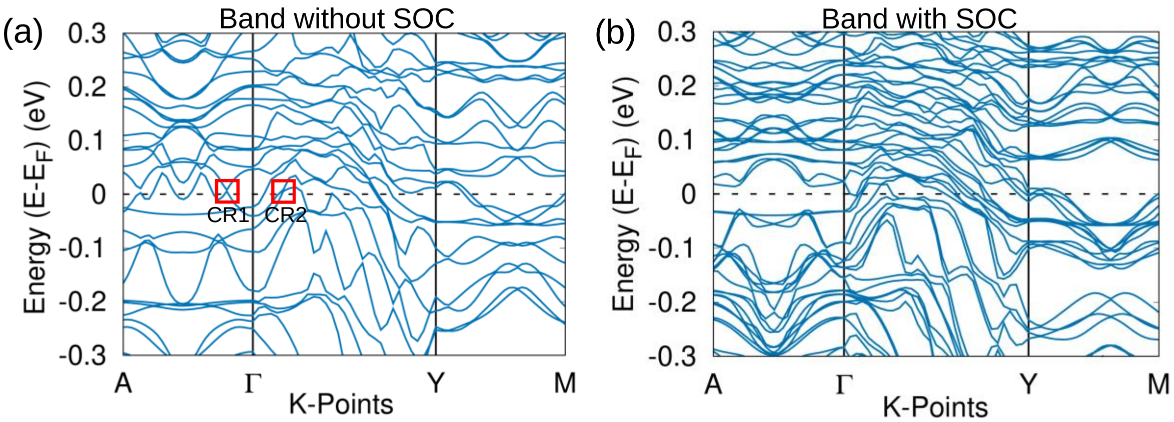

Fig. S3 Band structures (a) without, (b) with spin-orbit coupling (SOC) of $(BiSe)_{1.23}CrSe_2$.

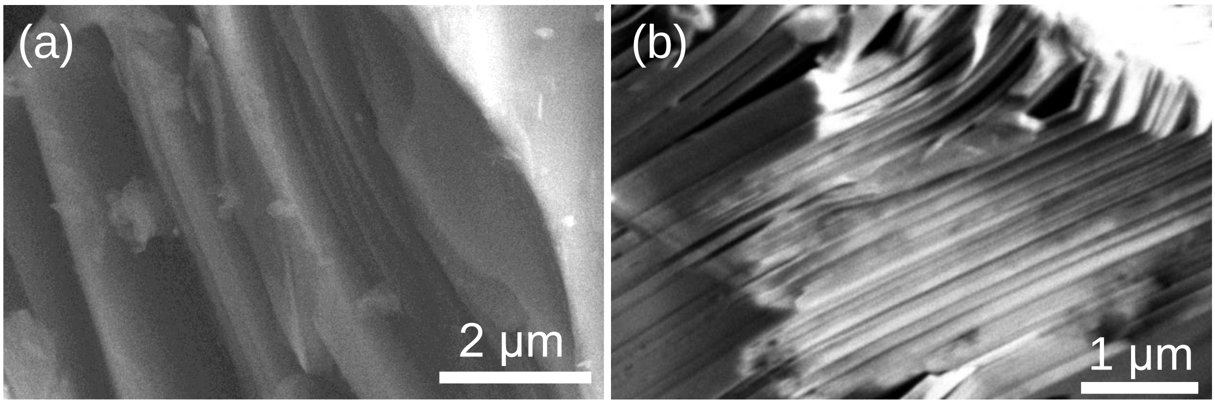

Fig. S4 (a) and (b) FE-SEM images of $(BiSe)_{1.23}CrSe_2$ MLC taken in back scattered mode (BSE) showing no distinct contrast differences.

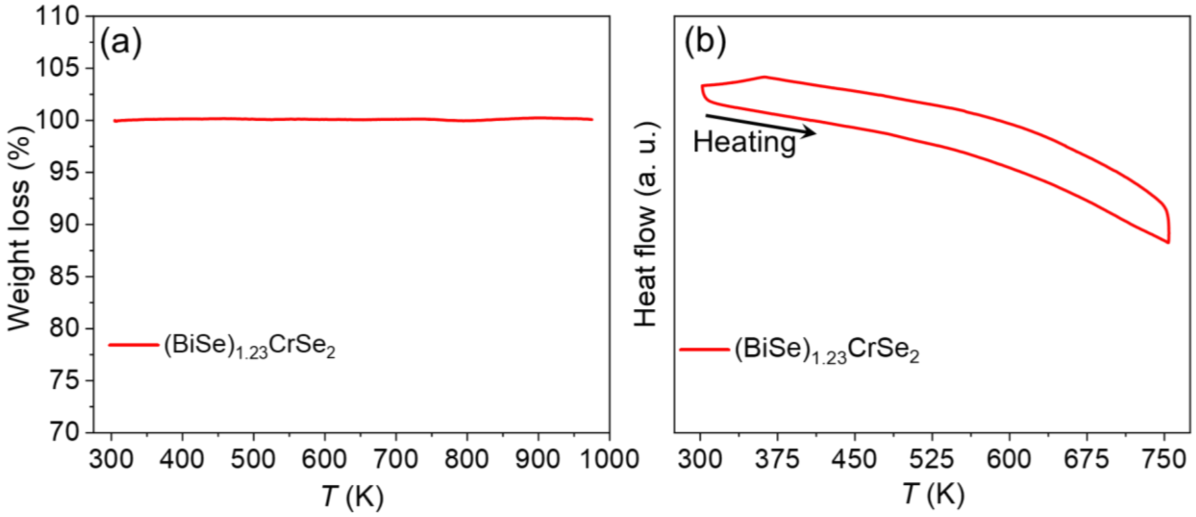

Fig. S5 (a) and (b) present the TGA and DSC curves, respectively, showing thermal stability of the $(BiSe)_{1.23}CrSe_2$ misfit layered compound (MLC).

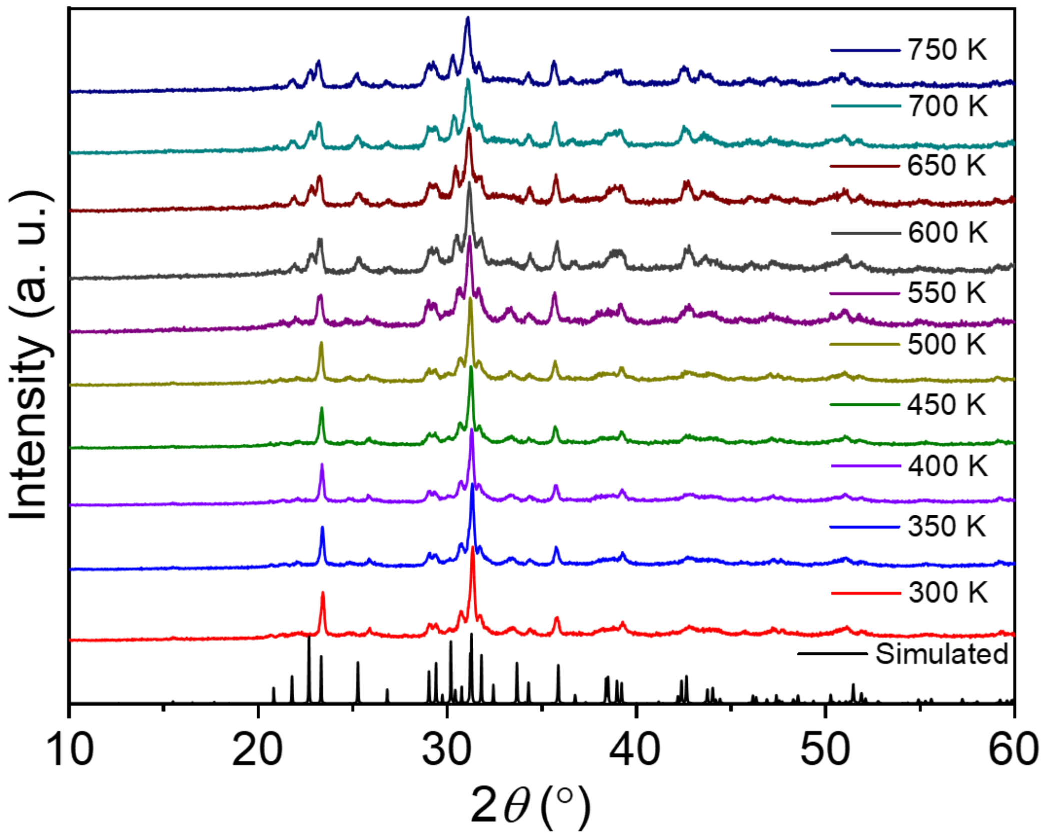

Fig. S6 Temperature dependence of $(BiSe)_{1.23}CrSe_2$ MLCs' PXRD pattern with the simulated pattern showing stability of the material at elevated temperatures, which is in good agreement with the observations from TGA and DSC.

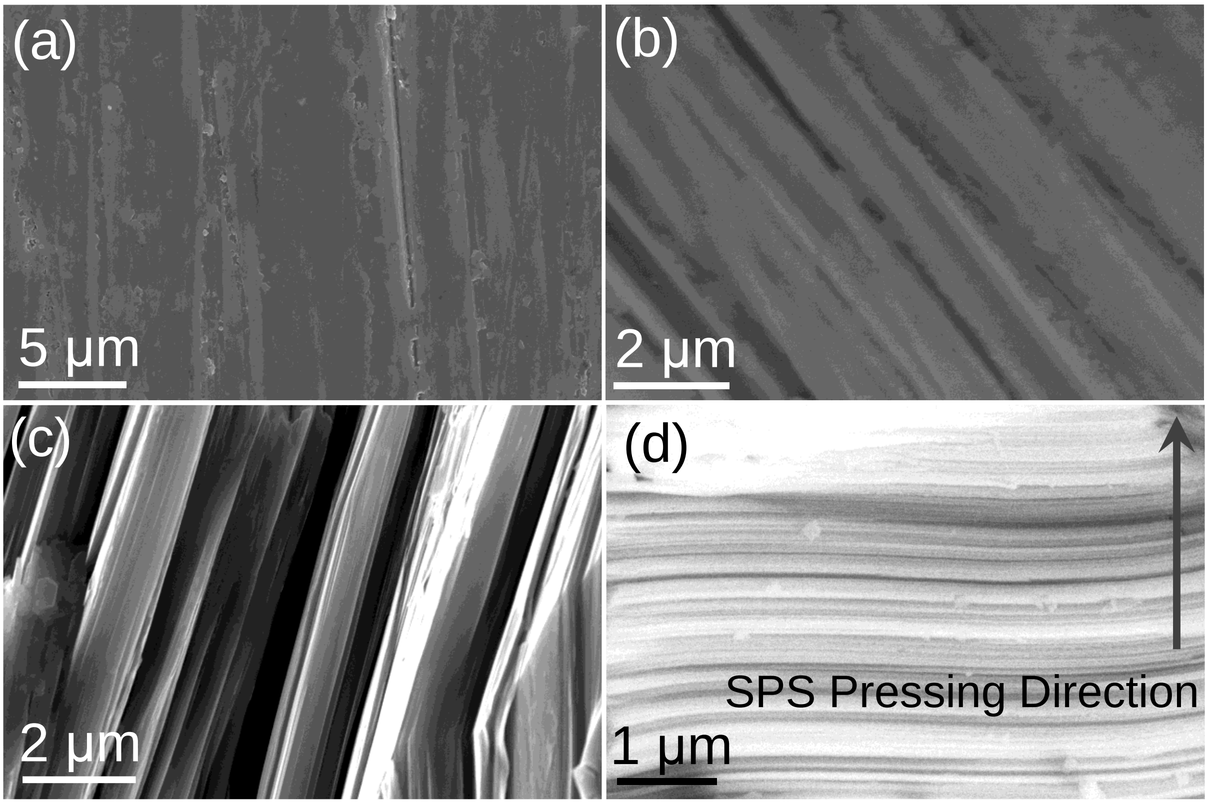

Fig. S7 a) Typical FESEM micrograph of the polished pellet, b) FESEM micrograph of the pellet recorded in backscattered electron mode corroborates the retention of single phase, and (c-d) FESEM micrographs of the cracked surface recorded in secondary and backscattered electron modes, respectively, showing the layered nature.

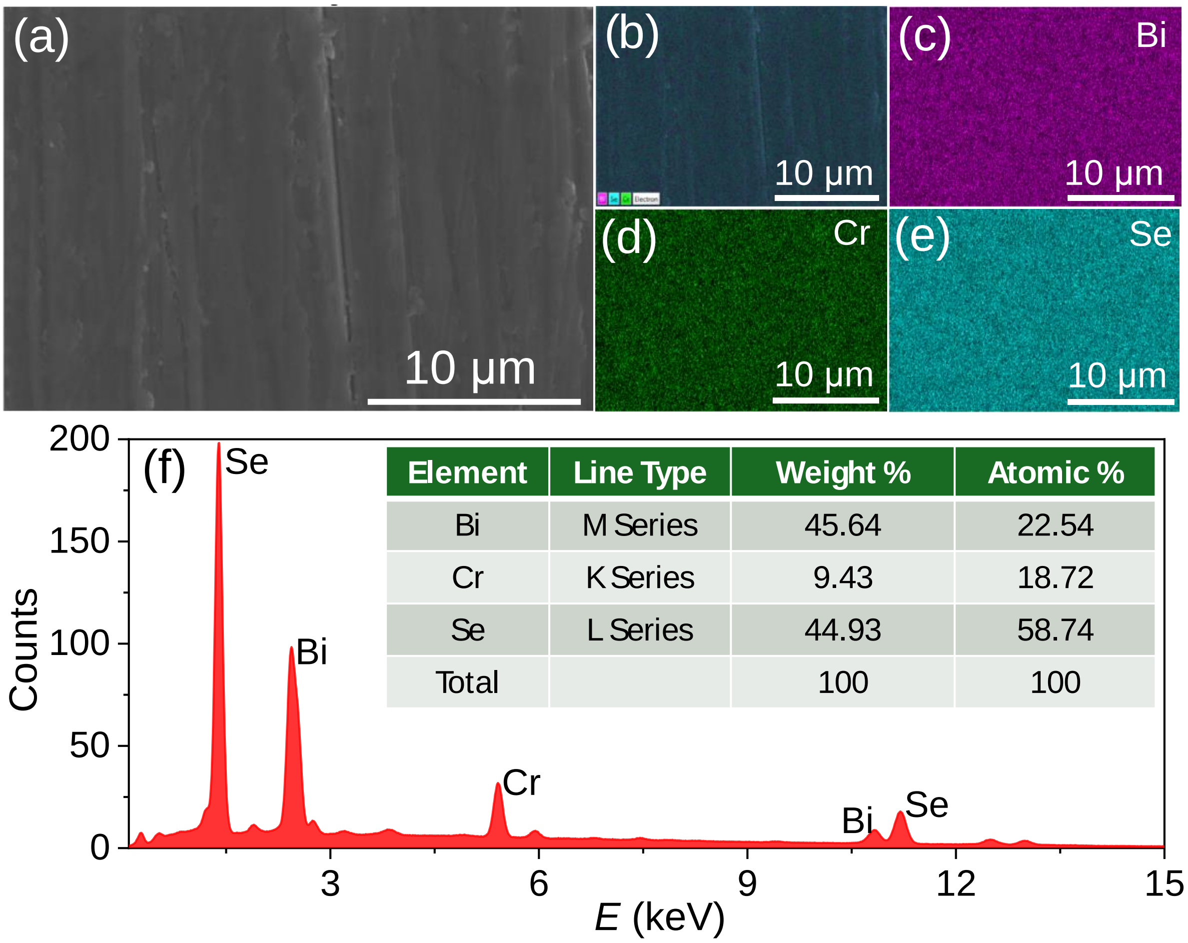

Element	Line Type	Weight %	Atomic %
Bi	M Series	45.64	22.54
Cr	K Series	9.43	18.72
Se	L Series	44.93	58.74
Total		100	100

Fig. S8 (a) FESEM micrograph of the polished pellet selected for the Energy Dispersive X-ray Spectroscopy (EDS), (b-e) EDS elemental mapping showing the uniform distribution of the constituent elements, and (f) the corresponding EDS spectrum, insert showing the quantified elemental composition.

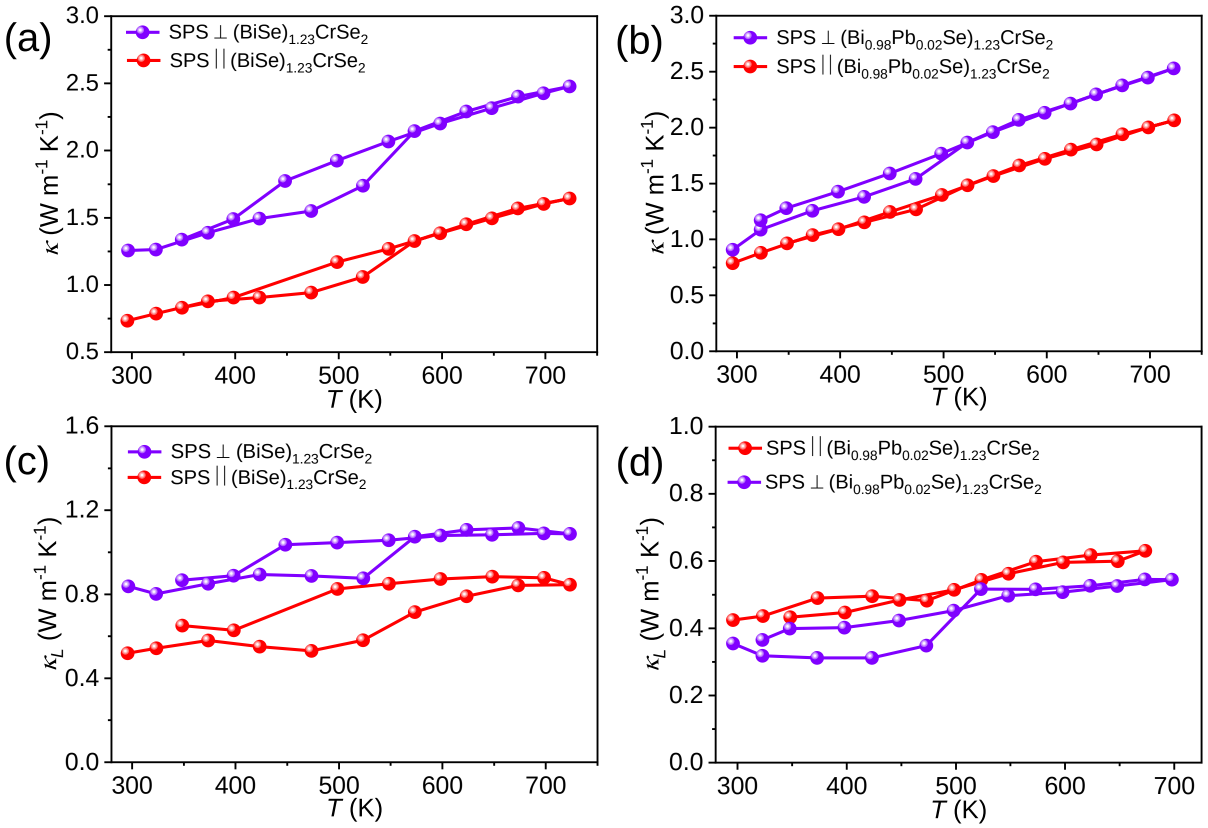

Fig. S9 Temperature dependent behaviour during heating-cooling cycles for (a) total thermal conductivity (κ) and (c) lattice thermal conductivity (κ_L) of the pristine $(BiSe)_{1.23}CrSe_2$, measured parallel and perpendicular to the SPS pressing direction, showing a pronounced hysteresis between 400 to 570 K. Upon 2% Pb-doping, a significant decrease in the hysteresis is seen κ (b) and κ_L (d).

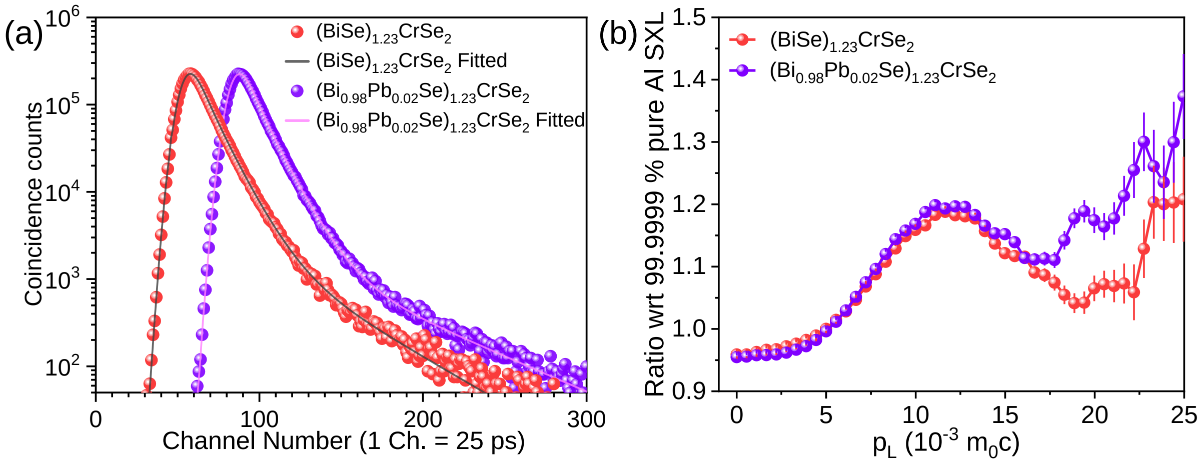

Fig. S10 (a) Room-temperature positron lifetime spectra of pristine and Pb-doped $(BiSe)_{1.23}CrSe_2$. The solid lines represent fits used to determine the positron lifetime components. (b) The area normalised point by point ratio between the CDB spectra of pristine and Pb-doped $(BiSe)_{1.23}CrSe_2$ with the CDB spectra of defect-free 99.9999 % pure aluminium.

Positron studies can provide insight into defects and are helpful in understanding the role of defects in transport. The positron annihilation lifetime spectrum (Figure S10a) of the Pristine and Pb-doped samples has been best fitted (using PATFIT 88 computer code) with three lifetime components. Table S1 presents the various lifetime components and their corresponding intensities. The source component measured with a pure aluminium and pure silicon sample has been well taken care of during the extraction of lifetime components. It shows a very long lifetime component of 996 ps to 1341 ps with an intensity of 3 %. This is a common phenomenon in polycrystalline samples. The origin of such a long component is the pick-off annihilation process, i.e., a positron initially forms an ortho-positronium (spin triplet state) with an electron and subsequently decays with another electron with opposite spin as para-positronium (spin singlet state). The intermediate lifetime component (τ_2) represents the lifetime of the positrons annihilating in a cation defect site. The value of the intermediate lifetime component has been increased from 288 ± 4 ps to 303 ± 5 ps, but its intensity (I_2) decreases from 78 % to 69 % due to the doping of Pb at the Bi site in $(BiSe)_{1.23}CrSe_2$. The present experimental result suggests the reduction of cation vacancy in the $(BiSe)_{1.23}CrSe_2$ due to the doping of lead. The shortest lifetime component, τ_1, is the free annihilation of positron at the bulk of the sample, which is also increased from 141 ± 3 to 159 ± 4 ps.

Table S1 Different lifetime components and their intensities.

Sample	**τ_1 (ps)**	**I_1 (%)**	**τ_2 (ps)**	**I_2 (%)**	**τ_3 (ps)**	**I_3 (%)**
$(Bi_{0.98}Pb_{0.02}Se)_{1.23}CrSe_2$	159 ± 4	28 ± 2	303 ± 5	69 ± 2	1341 ± 30	3 ± 0.2
$(BiSe)_{1.23}CrSe_2$	141 ± 3	19 ± 1	288 ± 4	78 ± 1	996 ± 30	3 ± 0.2

The coincidence Doppler broadening (CDB) spectroscopy has been employed to understand the chemical nature of the defect. The CDB data has been analysed by constructing a ratio curve. In the present case, the ratio curve has been constructed between the area-normalised CDB spectra of the $(BiSe)_{1.23}CrSe_2$ and $(Bi_{0.98}Pb_{0.02}Se)_{1.23}CrSe_2$ sample with respect to the area-normalised CDB spectra of a 99.9999 % pure aluminium sample. The coincidence Doppler broadening spectra of the $(BiSe)_{1.23}CrSe_2$ and $(Bi_{0.98}Pb_{0.02}Se)_{1.23}CrSe_2$ sample have been constructed with the CDB spectra of a defect-free 99.9999 % pure aluminium single crystal (Fig. S10b). In the figure, we find a peak around the momentum value 12.5×10^{-3} m_oc. In the positron annihilation process, just before annihilation, positrons are thermalised, i.e., their energy is in the order of meV, but the annihilating electrons have some kinetic energy. The kinetic energy of the electron, E_k, can be estimated using the Virial approximation[2] (in the atom, the expectation value of the kinetic energy of an electron, E_{kin}, is equal to the binding energy of the electron), as $E_k = p_L^2 / 2m_o$. Considering the momentum value of 12.5×10^{-3} m_oc, the corresponding kinetic energy of the electron has been calculated as 40 eV. It is also clear from Fig. S10b that the peak height increases due to the doping of lead $[(Bi_{0.98}Pb_{0.02}Se)_{1.23}CrSe_2]$ in $(BiSe)_{1.23}CrSe_2$. The 40 eV kinetic energy is very close to the 3*p* electron of chromium (Cr 3*p* ~ 42 eV).[3] Also, from Figure S10b, it is clearly seen that around 19×10^{-3} m_oc momentum value, the ratio curve for $(Bi_{0.98}Pb_{0.02}Se)_{1.23}CrSe_2$ has a higher value than the $(BiSe)_{1.23}CrSe_2$ sample. The momentum value of 19×10^{-3} m_oc corresponds to 92 eV, which is close to the 5*p* electron energy of Bismuth (92 eV) and 5*p* electrons of lead (83 eV). It suggests that positrons annihilate more readily with the 5*p* electrons of bismuth or lead. Thus, the present CDB ratio curve analysis, along with the positron lifetime data, suggests a reduction of cation vacancy (V_{Cr} and V_{Bi}) in $(BiSe)_{1.23}CrSe_2$ after doping of Pb at the bismuth site, i.e., in $(Bi_{0.98}Pb_{0.02}Se)_{1.23}CrSe_2$.

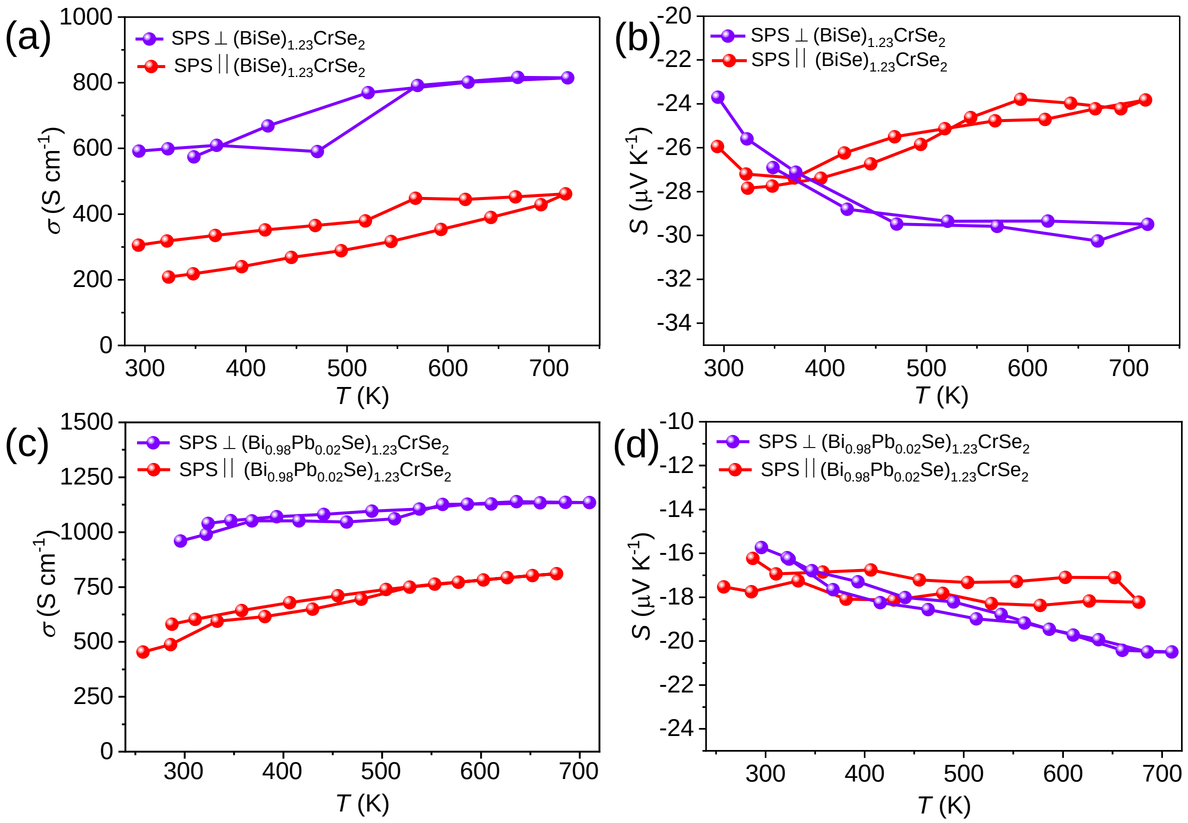

Fig. S11 Temperature dependence of electrical conductivity (σ) and Seebeck coefficient (S) of pristine (a-b) and Pb-doped (c-d), measured parallel and perpendicular to the SPS pressing direction.

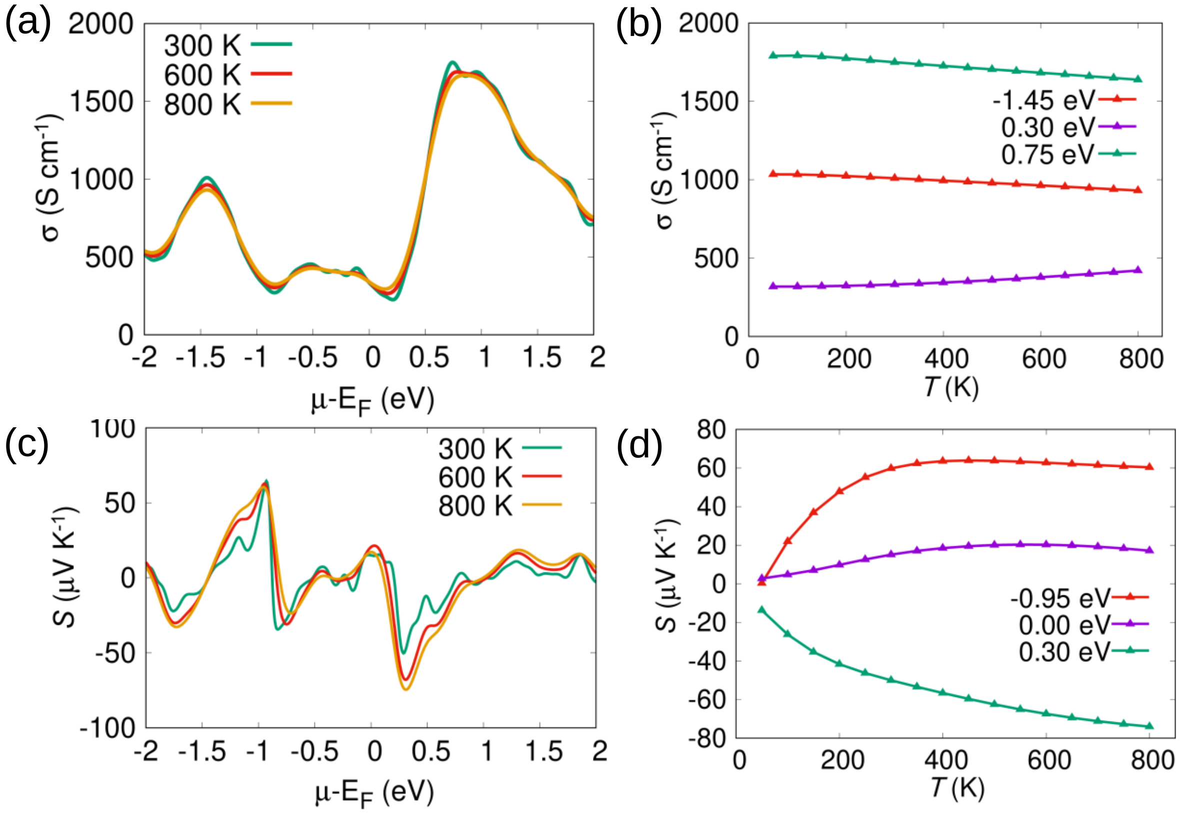

Fig. S12 Chemical potential (μ) and temperature-dependent (a)-(b) electrical conductivities (σ) and (c)-(d) Seebeck coefficient (S) in $(BiSe)_{1.23}CrSe_2$. Here, the Fermi level is denoted by E_F.

Theoretical analysis of the electrical transport properties of $(BiSe)_{1.23}CrSe_2$, specifically electrical conductivity and Seebeck coefficient, has been performed to interpret the experimentally observed thermoelectric response. Figure S12(a)-(d) shows theoretically estimated responses in $(BiSe)_{1.23}CrSe_2$. The electronic structure of $(BiSe)_{1.23}CrSe_2$ shows multiple conduction band pockets at different energies and linearly dispersing bands (Fig. S3 and Fig. 1c). Therefore, we also scan the electrical responses in $(BiSe)_{1.23}CrSe_2$ with chemical potential around the Fermi level (E_F), as shown in Figure S12 (a) and (c), respectively. The Seebeck coefficient changes its character from *n* (negative) type to a *p* (positive) type conduction with chemical potentials (μ) as shown in Figure S12(d). Although the band structure of the compound shows metallic, the conductivity of the sample is much lower than that of typical metals. The electrical conductivity increases with temperature in the *n*-type region of $(BiSe)_{1.23}CrSe_2$ for μ = 0.3 eV (Figure S12b), which is consistent with experimentally observed trends (Figure S11a). Such behaviour can be attributed to the contribution from a thermally activated semiconducting transport mechanism. At low temperatures, a significant fraction of donor states and Cr-3*d* localised states remain un-ionised, resulting in a limited population of mobile electrons. As the temperature rises, thermal energy progressively ionises these donor levels and promotes electrons from localised states into extended conduction-band states, thereby increasing the carrier concentration. Rising temperature also weakens the localisation induced by the misfit-layered structure and Cr-3*d* magnetic interactions. This enables electrons to transit more easily into extended states, which also increases electronic population in band pockets and improves hopping or band-like transport. Together, these effects result in a monotonic increase in conductivity with temperature, consistent with n-type semiconductor behaviour.

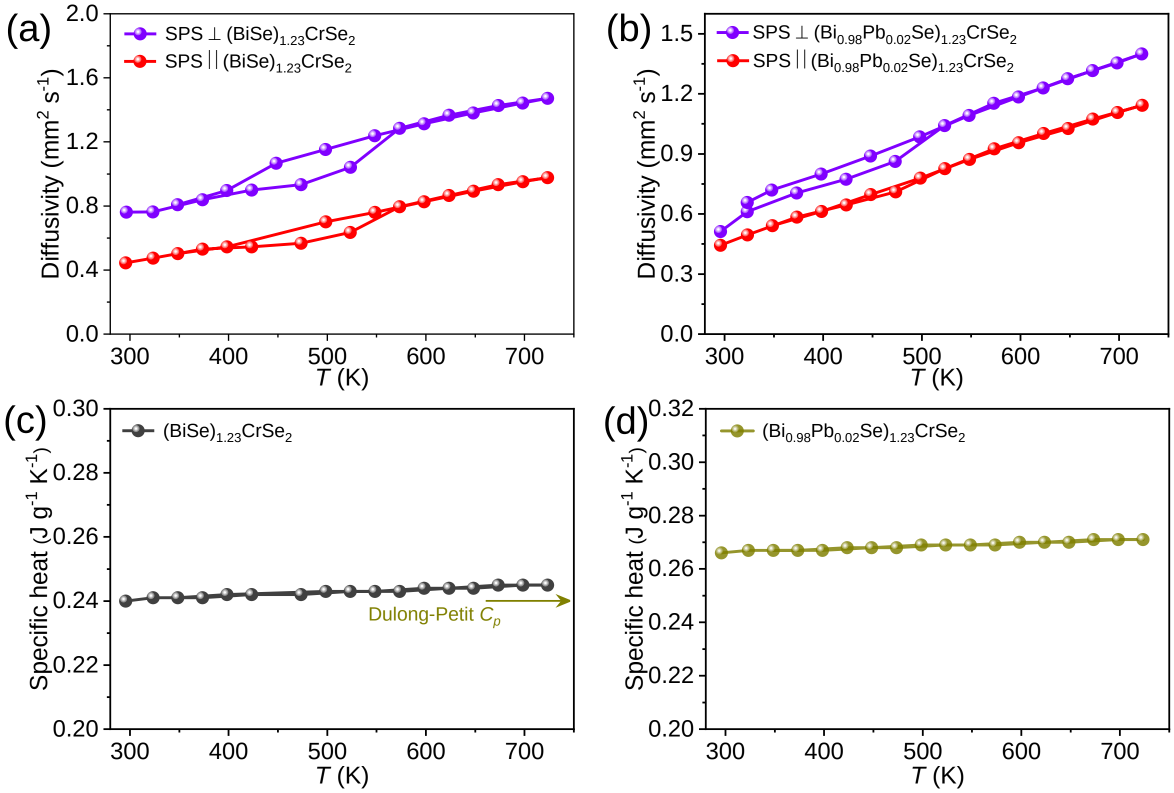

Fig. S13 Temperature dependence of thermal diffusivity of pristine (a) and Pb-doped (b), measured parallel and perpendicular to the SPS pressing direction, along with the temperature dependence of specific heat for pristine (c) and Pb-doped (d) samples. The specific heat estimated from the Dulong–Petit limit is ~ 0.24 J g^{-1} K^{-1}.

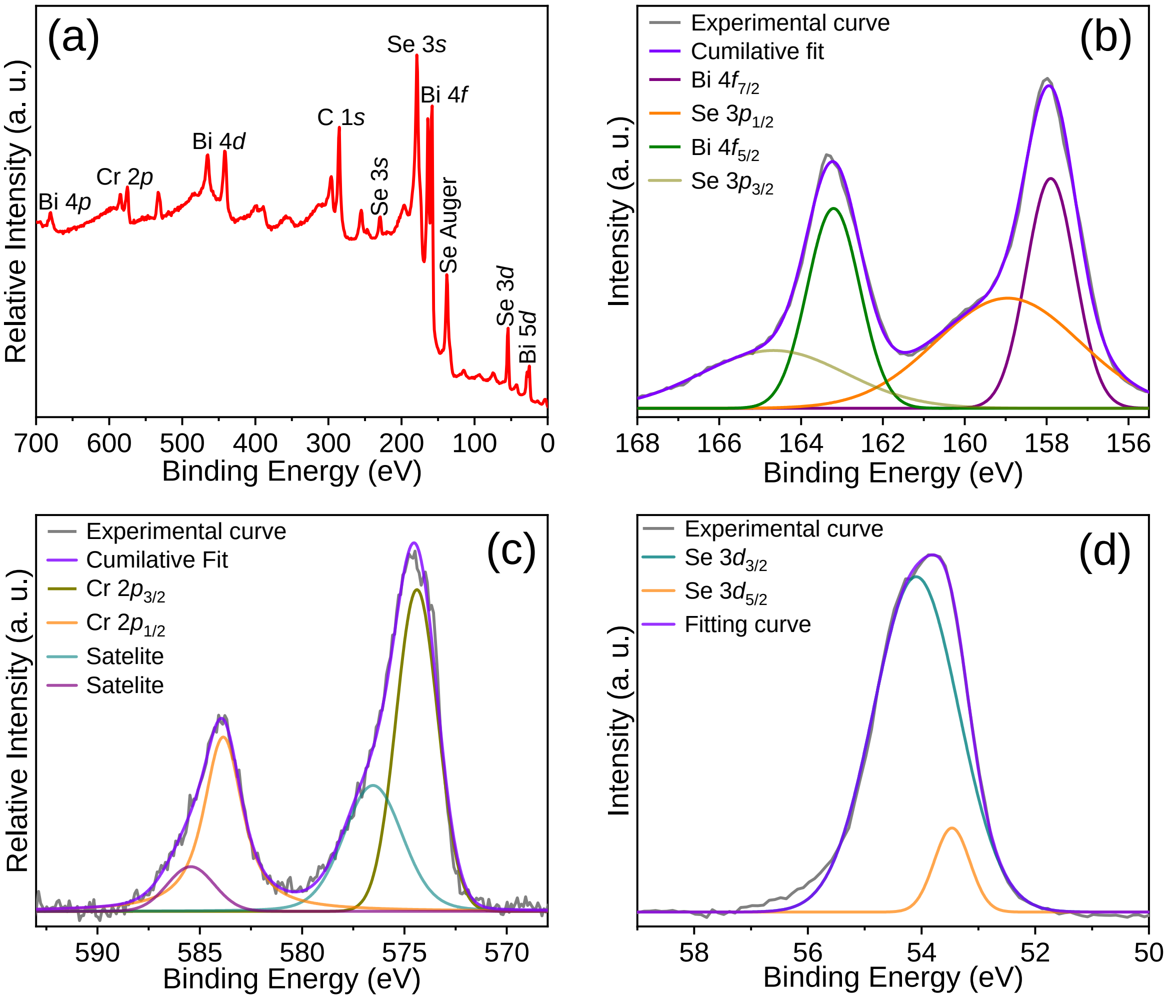

Fig. S14 X-ray photoelectron spectroscopy (XPS) analysis of as-synthesised (BiSe)$_{1.23}$CrSe$_2$: (a) Survey spectrum. (b) High-resolution Bi 4f spectrum, showing two distinct peaks at binding energies of 157.89 eV and 163.20 eV with a splitting of 5.31 eV, corresponding to the spin-orbit coupled Bi 4$f_{7/2}$ and Bi 4$f_{5/2}$, respectively. (c) High-resolution Cr 2p spectrum, revealing two peaks at 574.38 eV and 583.85 eV (separation 9.47 eV), assigned to Cr 2$p_{3/2}$ and Cr 2$p_{1/2}$, with satellite peaks arising from electronic contributions.[4] (d) High-resolution Se spectrum, displaying two peaks at 54.09 eV and 53.46 eV, corresponding to Se 3$d_{3/2}$ and Se 3$d_{5/2}$. The measured binding energies are in excellent agreement with XPS studies of single-crystalline (BiSe)$_{1.23}$CrSe$_2$.[1] All peaks were fitted using a Gaussian model, yielding excellent goodness-of-fit (R^2) values of 0.9974 (Bi), 0.9912 (Cr), and 0.9976 (Se).

Table S2 Measured sound velocities and the derived parameters of $(BiSe)_{1.23}CrSe_2$: minimum thermal conductivity (κ_{min}), diffusion thermal conductivity (κ_{diff}), Poisson ratio (ν_p) and Grüneisen parameter (γ).

Sample	Longitudinal sound velocity (m s^{-1})	Transverse sound velocity (m s^{-1})	Average sound velocity (m s^{-1})	Mean sound velocity (m s^{-1})	κ_{min} (W m^{-1} K^{-1})	κ_{diff} (W m^{-1} K^{-1})	ν_p	γ
$(BiSe)_{1.23}CrSe_2$ SPS ∥	2234	1119	1255	1281	0.3	0.2	0.33	2
$(BiSe)_{1.23}CrSe_2$ SPS ⊥	2406	1341	1493	1535	0.35	0.22	0.27	1.6

Table S3 Measured sound velocities of different misfit layered compounds.

Sample	Longitudinal sound velocities (ms^{-1})	Transverse sound velocities (ms^{-1})	Average sound velocity (ms^{-1})	Anisotropic ratio	Reference
$(BiSe)_{1.23}CrSe_2$ SPS ∥	2234	1119	1255	~1.2	This work
$(BiSe)_{1.23}CrSe_2$ SPS ⊥	2406	1341	1493		
$(LaS)_{1.14}NbS_2$ SPS ∥	4550	1920	2170	~1.06	5
$(LaS)_{1.14}NbS_2$ SPS⊥	3950	2060	2300		
$(La_{0.95}S_{0.95})_{1.14}NbS_2$ SPS ∥	4890	2240	2530	~1.08	5
$(La_{0.95}S_{0.95})_{1.14}NbS_2$ SPS⊥	4830	2420	2720		
$(PbS)_{1.18}(TiS_2)_2$	3834	1120	1276		6
$(BiS)_{1.2}(TiS_2)_2$	3662	1350	1532		7
$(BiS)_{1.2}(Mg_{0.05}Ti_{0.95}S_2)_2$	3596	1429	1619		

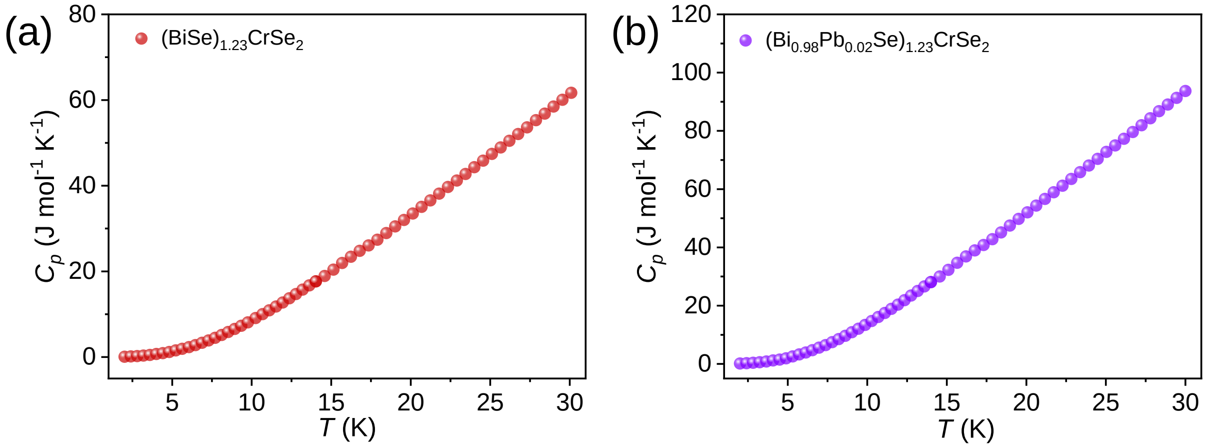

Fig. S15 Low-temperature heat capacity of (a) $(BiSe)_{1.23}CrSe_2$ and (b) $(Bi_{0.98}Pb_{0.02}Se)_{1.23}CrSe_2$.

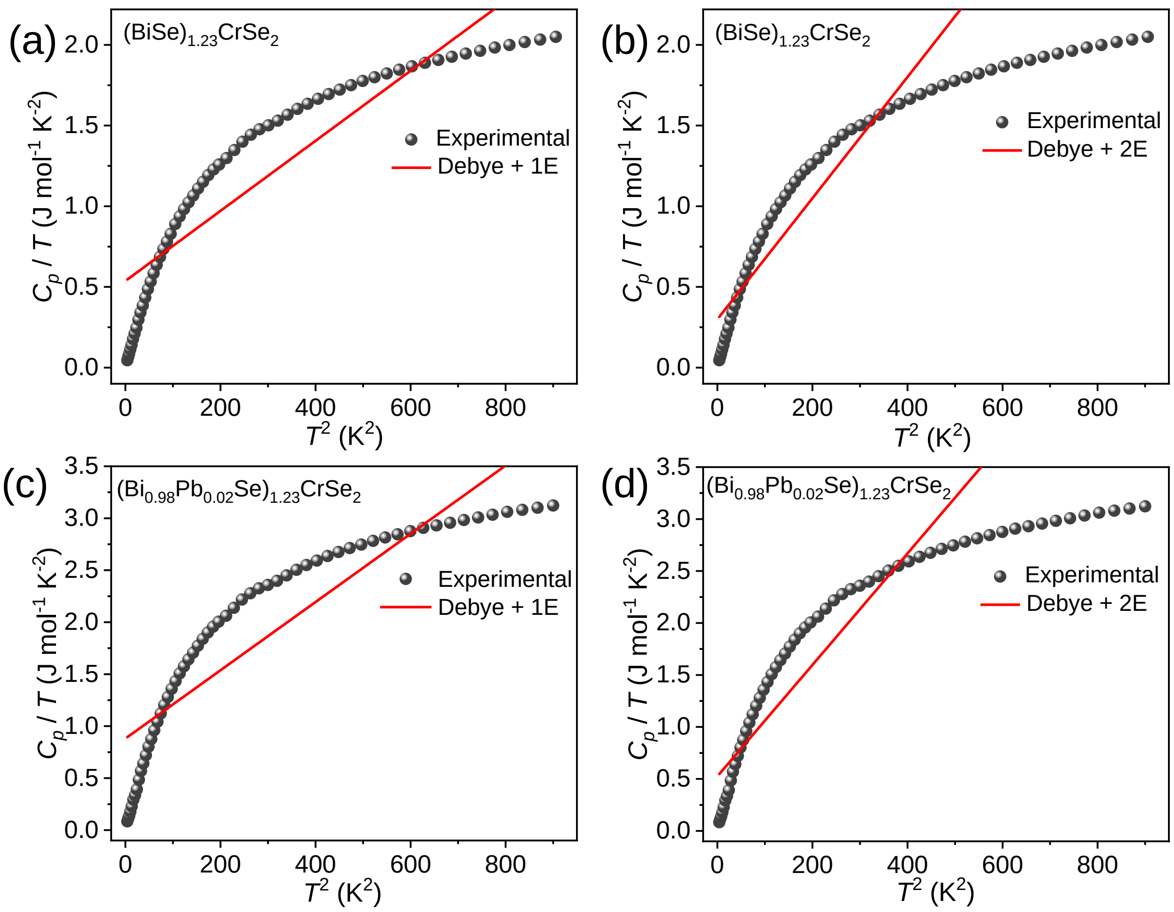

Fig. S16 Low temperature experimental C_p/T vs T^2 plot, fitted with the Debye-Einstein model, showing that more than two Einstein modes are required for reasonable fitting for Pristine (a-b) and Pb-doped (BiSe)$_{1.23}$CrSe$_2$ (c-d) MLC, respectively.

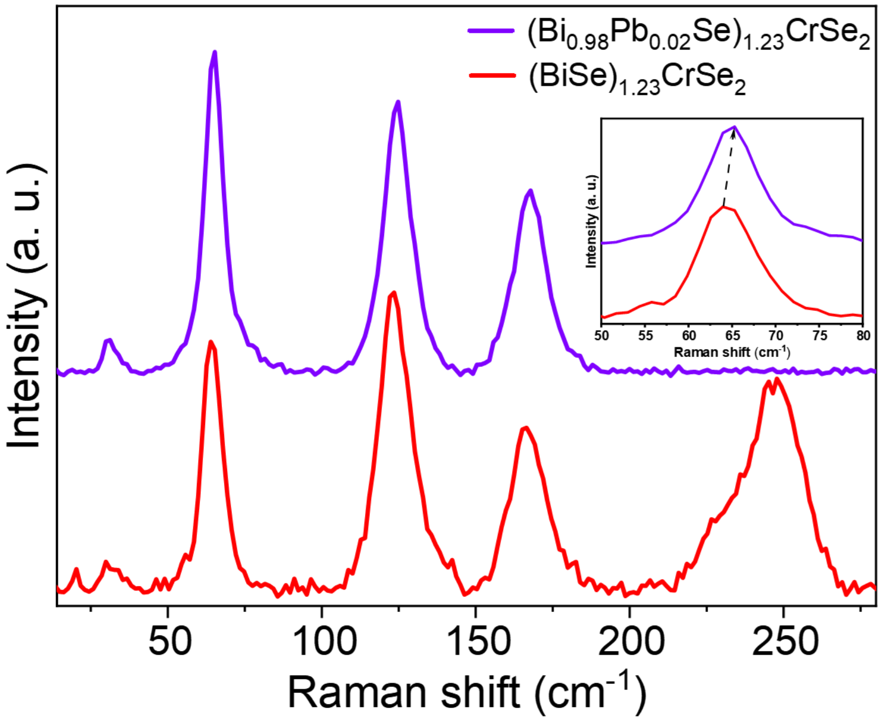

Fig. S17 Room-temperature Raman spectra of (a) $(BiSe)_{1.23}CrSe_2$ and (b) $(Bi_{0.98}Pb_{0.02}Se)_{1.23}CrSe_2$, inset showing the blue shift in peak position.

Table S4 The parameters for $(BiSe)_{1.23}CrSe_2$ and $(Bi_{0.98}Pb_{0.02}Se)_{1.23}CrSe_2$ obtained by fitting the experimental C_p/T vs T^2 data to a combined Debye-Einstein model.

Parameters	**Derived values for $(BiSe)_{1.23}CrSe_2$**	**Derived values for $(Bi_{0.98}Pb_{0.02}Se)_{1.23}CrSe_2$**
γ / J mol^{-1} K^{-2}	0.05621 ± 0.00377	0.09337 ± 0.00613
β / 10^{-4} J mol^{-1} K^{-2}	5.93035 ± 0.453383	7.7571 ± 1.27049
A_1 / J mol^{-1} K^{-1}	4.02127 ± 0.42074	66.3243 ± 9.64164
θ_{E1} / K	22.44317 ± 0.77688 (15.6 cm^{-1})	109.54025 ± 7.75853 (76.1 cm^{-1})
A_2 / J mol^{-1} K^{-1}	26.49516 ± 1.63767	48.34531 ± 3.91568
θ_{E2} / K	49.47666 ± 1.45385 (34.4 cm^{-1})	53.7527 ± 2.01061 (37.4 cm^{-1})
A_3 / J mol^{-1} K^{-1}	44.42172 ± 2.67093	9.14094 ± 1.06937
θ_{E3} / K	99.77767 ± 4.00951 (69.3 cm^{-1})	25.39153 ± 0.86513 (17.6 cm^{-1})
θ_D / K	~ 122	~ 87
R^2	0.99996	0.99994
χ^2	1.7564E-5	6.54183E-5

Table S5 Raman spectra fitting parameters for $(BiSe)_{1.23}CrSe_2$ and $(Bi_{0.98}Pb_{0.02})_{1.23}CrSe_2$, alongside the subsequently determined phonon lifetimes (τ_i). The corresponding goodness-of-fit (R^2) values are 0.9856 and 0.9879.

Sample	Raman Mode (cm^{-1})	FWHM (cm^{-1})	τ_i (ps)
$(BiSe)_{1.23}CrSe_2$	31.9	11.98	0.445
	64.4	7.75	0.688
	123.6	11.78	0.452
	166.1	13.04	0.408
$(Bi_{0.98}Pb_{0.02}Se)_{1.23}CrSe_2$	31.01	4.33	1.225
	69.99	6.79	0.782
	124.48	9.03	0.589
	167.75	10.69	0.497

Table S6 Room-temperature lattice thermal conductivity (κ_L), minimum lattice thermal conductivity (${\kappa_L}^{min}$) and phonon lifetime (τ_i) of low thermal conductivity, and a high thermal conductivity material, MoS_2.

Compound	**κ_L at RT (W m^{-1} K^{-1})**	**Measured ${\kappa_L}^{min}$ (W m^{-1} K^{-1})**	**τ_i (ps)**	**Ref.**
$(BiSe)_{1.23}CrSe_2$	~ 0.52	~ 0.52	0.4 – 0.68	This work
$(Bi_{0.98}Pb_{0.02}Se)_{1.23}CrSe_2$	~ 0.35	~ 0.31	0.49 – 1.22	This work
$TlCuZrSe_3$	~ 0.88	~ 0.41	0.9 – 1.1	[8]
$Bi_{1.1}Sb_{0.9}Te_2S$	~0.6	~0.46	0.3-1	[9]
$Cu_{1-x}\square_xPb_{1-x}Bi_{1+x}S_3$	~0.55	~0.48	0.41	[10]
$AgErTe_2$	~0.64	~0.3	0.7	[11]
$Cu_{1.6}Bi_{4.8}S_8$	~ 0.71	~ 0.44	2 – 4.5	[12]
$WS_{1.8}Se_{0.2}$	~1	~0.6	0.55-1.1	[13]
Cs_2SnI_6	~0.37	~0.28	1.04 – 1.83	[14]
$Cs_2NaInCl_6$	~0.43	~0.43	0.4-0.85	[15]
$Cs_3Bi_2I_6Cl_3$	~0.2	~0.2	0.5 – 1	[16]
MoS_2	~23.2	-	38	[17]

References

1 S. M. Clarke and D. E. Freedman, *Inorg. Chem.*, 2015, **54**, 2765–2771.

2 U. Myler and P. J. Simpson, *Phys. Rev. B*, 1997, **56**, 14303–14309.

3 https://www.webelements.com. (accessed 14 Feb 2026).

4 Q. Lu, *ACS Nano*, 2024, **18**, 13973–13982.

5 P. Jood, M. Ohta, O. I. Lebedev and D. Berthebaud, *Chem. Mater.*, 2015, **27**, 7719–7728.

6 C. Wan, Y. Wang, N. Wang and K. Koumoto, *Materials*, 2010, **3**, 2606–2617.

7 Y. E. Putri, C. Wan, Y. Wang, W. Norimatsu, M. Kusunoki and K. Koumoto, *Scr. Mater.*, 2012, **66**, 895–898.

8 R. K. Rohj, A. Bhui, S. Sett, A. Ghosh, K. Biswas and D. D. Sarma, *Chem. Mater.*, 2025, **37**, 520–529.

9 R. Pathak, P. Dutta, A. Srivastava, D. Rawat, R. K. Gopal, A. K. Singh, A. Soni and K. Biswas, *Angew. Chem. Int. Ed.*, 2024, **63**, e202408908.

10 V. Carnevali, S. Mukherjee, D. J. Voneshen, K. Maji, E. Guilmeau, A. V. Powell, P. Vaqueiro and M. Fornari, *J. Am. Chem. Soc.*, 2023, **145**, 9313–9325.

11 D. Sarkar, S. Shahabfar, Y. Liu, P. Yanda, T. S. Ie, H. Zhao, P. Nandi, K. R. Pradeep, C. Shekhar, C. Felser, V. P. Dravid, C. M. Wolverton and M. G. Kanatzidis, *J. Am. Chem. Soc.*, 2025, **147**, 46483–46496.

12 A. Bhui, M. Dutta, M. Mukherjee, K. S. Rana, A. K. Singh, A. Soni and K. Biswas, *Chem. Mater.*, 2021, **33**, 2993–3001.

13 M. T, V. Vijay, J. Archana, M. Navaneethan and K. D. Nisha, *Surfaces and Interfaces*, 2025, **72**, 106905.

14 A. Bhui, T. Ghosh, K. Pal, K. Singh Rana, K. Kundu, A. Soni and K. Biswas, *Chem. Mater.*, 2022, **34**, 3301–3310.

15 G. Wang, J. Zheng, J. Xue, Y. Xu, Q. Zheng, G. Hautier, H. Lu and Y. Zhou, *Adv. Sci.*2025, **12**, 2408149.

16 P. Acharyya, T. Ghosh, K. Pal, K. S. Rana, M. Dutta, D. Swain, M. Etter, A. Soni, U. V. Waghmare and K. Biswas, *Nat. Commun.*, 2022, **13**, 5053.

17 Y. Cai, J. Lan, G. Zhang and Y. W. Zhang, *Phys. Rev. B*, 2014, **89**, 035438.